Nanoscale Advances

ROYAL SOCIETY OF CHEMISTRY

PAPER

View Article Online
View Journal | View Issue

Cite this: *Nanoscale Adv.*, 2021, **3**, 3502

PEDOT:PSS-glued MoO_3 nanowire network for all-solid-state flexible transparent supercapacitors†

Jie Liang,[a] Hongwei Sheng,[a] Qi Wang,[a] Jiao Yuan,[a] Xuetao Zhang,[a] Qing Su,[a] Erqing Xie,[a] Wei Lan *[a] and Chuanfang (John) Zhang *[b]

Flexible transparent supercapacitors (FTSCs) are essential for the development of next-generation transparent electronics, however, a significant challenge is to achieve high-areal-capacitance FTSCs without sacrificing optical transparency. Herein, poly(3,4-ethylene dioxythiophene):poly(styrene sulfonate) (PEDOT:PSS)-glued MoO_3 nanowires anchored on the Ag nanofiber (AgNF) network are employed as FTSC film electrodes, in which the AgNF network provides primary conducting pathways and guarantees rapid electron transport, while wide-bandgap semiconductor MoO_3 nanowires glued by the ultrathin PEDOT:PSS layer provide abundant redox-active sites to store energy. Benefiting from the PEDOT:PSS as the conducting glue to promote the connection at the junctions between AgNFs and MoO_3 nanowires, the as-prepared AgNFs/MoO_3/PEDOT:PSS (AMP) film electrode demonstrates a high transmittance (82.8%) and large areal capacitance (15.7 mF cm^{-2}), and has outperformed all the transparent conductive films known to date. Even after 11 000 charge/discharge cycles, the capacitance still remains at 92.4% of the initial value. The assembled all-solid-state FTSC device delivers an energy density of 0.623 μW h cm^{-2}, a power density of 40 μW cm^{-2}, and excellent mechanical robustness, implying a great potential in high performance FTSCs.

Received 15th February 2021
Accepted 13th April 2021

DOI: 10.1039/d1na00121c

rsc.li/nanoscale-advances

1. Introduction

With the ever-growing demand for flexible transparent electronics, it is of great significance to develop flexible, transparent energy storage devices with high-energy-density.[1–4] Compared with other energy storage devices,[5–10] supercapacitors are a promising candidate for flexible and transparent applications due to their long lifetime and high power density.[11–17] In general, high transparency can be achieved by thinning down the thickness of electrodes to the nanoscale. This inevitably interrupts the continuous conductive network and raises the so-called percolation problem. In other words, electrodes typically experience a sharply-increased sheet resistance when further reducing the film thickness beyond the threshold.[18] As such, both the electron transport across the thin film and the achievable transmittance of the electrode are limited, leading to much compromised optoelectronic and electrochemical properties in the resultant supercapacitors. Indeed, the major challenges in the transparent supercapacitor field include but not limited to (1) too low areal capacitance typically around 0.5 mF cm^{-2} despite the devices being opaque (T <60%) and (2) poor mechanical flexibility and stability due to the weakly-bonded junctions. To develop advanced transparent supercapacitors, both the areal capacitance (C_A) and transparency (T) of the electrode should be maximized, corresponding to a high figure of merit (FoM_c), defined as the ratio of C_A to optical conductivity (σ_{op}).[19]

To this end, extensive efforts have been devoted to constructing advanced film electrodes with rational design on transparent conductive networks. For instance, highly conductive ultrathin films based on graphene,[13,20] carbon nanotubes,[21–23] MXenes,[24–28] and conductive polymers[12,29] have been reported as both current collectors and active materials. Typically, FTSC electrodes consist of a capacitive (or pseudocapacitive) material (such as MnO_2,[30] polypyrrole (PPy),[31,32] and $Co(OH)_2$[33]) supported on a percolative metallic network[34] (such as Au/Ag nanofibers,[35,36] Au/Ag nanowires,[37] and Ni/Au mesh,[14]). Such a configuration allows efficient charge transport and smooth surface redox reactions, providing maximal areal capacitance for transparent electrodes. For example, Kiruthika *et al.* fabricated a transparent solid-state supercapacitor using an electrodeposited Au/MnO_2 network with an areal capacitance of 0.66 mF cm^{-2} and optical transparency of 63%.[38] We previously reported an ultrathin, vertically aligned, $Co(OH)_2$ nanosheets/Ag nanowire hybrid network for FTSCs, which demonstrated an areal capacitance of 0.9 mF cm^{-2} at 54%

[a]*Key Laboratory of Special Function Materials and Structure Design, Ministry of Education, School of Physical Science and Technology, Lanzhou University, Lanzhou, 730000, People's Republic of China. E-mail: lanw@lzu.edu.cn*

[b]*Laboratory for Functional Polymers, Empa, Swiss Federal Laboratories for Materials Science and Technology, ETH Domain, Überlandstrasse 129, Dübendorf, CH-8600, Switzerland. E-mail: chuanfang.zhang@empa.ch*

† Electronic supplementary information (ESI) available. See DOI: 10.1039/d1na00121c

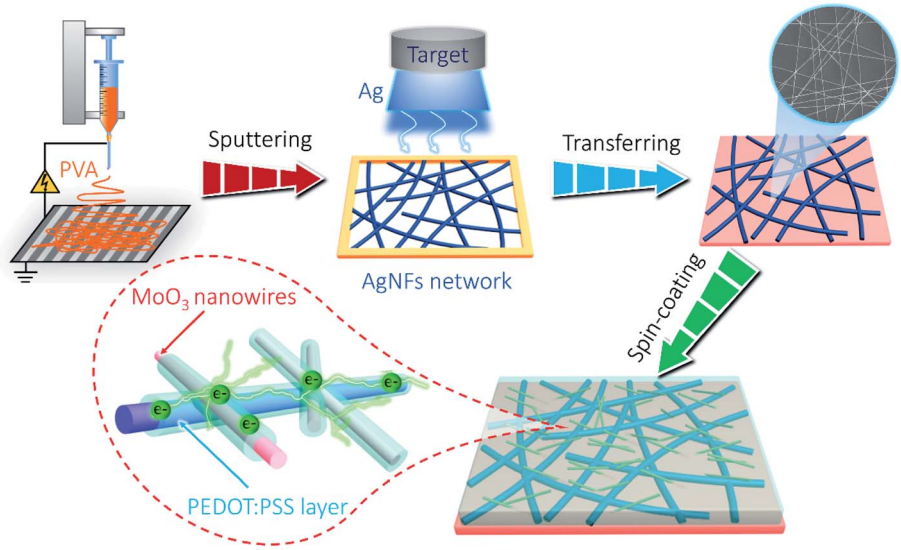

Scheme 1 The fabrication schematic of AMP film electrodes.

transmittance and excellent cycling stability (91% retention after 10 000 charge/discharge cycles).[2] Recently, Chen *et al.* developed an FTSC device based on a quasifractal electrode structure by copying leaf venation, exhibiting an areal capacitance of 5.6 mF cm^{-2} (at 45% transparency), and only 2500 cycles of charging/discharging process.[39] These reports, however, suggest a relatively low FoM_c for the transparent supercapacitor system. In other words, ideal transparent supercapacitors require both high areal capacitance and high transparency achieved at the same time, which has proven to be quite challenging.

Oxides are widely used in various fields.[40] Orthorhombic molybdenum trioxide (MoO_3) is an oxide semiconductor with a bandgap of 3.1 eV, allowing visible light to pass through and thus it can be used for transparent functional devices. MoO_3 has a unique laminated structure with MoO_6 octahedrons as the basic building units, being suitable for intercalation/de-intercalation of small ions, such as H^+ and Li^+ ions. Therefore, one-dimensional (1D) MoO_3 nanowires possess a high theoretical specific capacitance (1256 F g^{-1}) and large surface area. However, its low electrical conductivity limits the transport of electrons in the MoO_3 nanowire network. Said otherwise, 1D MoO_3 has to be deposited on transparent current collectors such as poly(3,4-ethylene dioxythiophene):poly(styrene sulfonate) (PEDOT:PSS).[18,41,42] In particular, the Ag nanofiber (AgNF) based percolative network exhibits a high transmittance coupled with low sheet resistances. Compared to the percolative networks composed of quasifractal structures and metal nanowires,[2,38,39] AgNF network-based transparent current collectors possess an intrinsic low percolation threshold due to the ultrahigh aspect ratio in the decimeter-long nanowires with hundreds of nanometers in diameter. Consequently, the junction resistance which determines the sheet resistance of the transparent current collectors can be minimized. Depositing 1D MoO_3 onto the AgNF network is expected to achieve highly transparent electrodes with high areal capacitance. However, the poor adhesion of MoO_3 nanowires to AgNFs strongly limits the mechanical flexibility of the resultant electrodes, as well as enlarging the junction resistance, leading to much compromised optoelectronic and electrochemical performances.

Herein, we aim to solve this issue by introducing PEDOT:PSS as the "conducting glue" to promote both the electron hopping kinetics at the junctions between AgNFs and MoO_3 nanowires, as well as the mechanical properties of the network (schematically shown in Scheme 1). Such a rational design simultaneously achieves excellent optoelectronic and electrochemical performances in the resultant AgNFs/MoO_3/PEDOT:PSS (AMP) based supercapacitor device, including high transparency and large capacitance, long-term electrochemical cycling stability, excellent mechanical robustness, *etc.*

2. Experimental

2.1. Materials

All chemicals were of analytical grade and used without further purification. Molybdenum powder (Mo, Tianjin Guangfu Technology Development Co. Ltd), hydrogen peroxide with 30 wt% (H_2O_2, Chengdu Kelong Chemical Reagent Factory), sodium sulfate (Na_2SO_4, Chengdu Kelong Chemical Reagent Factory), lithium chloride (LiCl, Chengdu Kelong Chemical Reagent Factory), polyvinyl alcohol (PVA1788, 99.0%, Sigma-Aldrich), PEDOT:PSS and polyethylene terephthalate (PET) substrates were used for electrode fabrication and electrochemical characterization. PEDOT:PSS (1.3–1.7 wt%) was purchased from Cool Chemical Tech Co., China. The high purity silver target (99.99%) was purchased from Sino Connaught New Material Tech Co., China.

2.2. Electrode preparation

2.2.1. Preparation of the AgNFs network. In a typical procedure, 2 g of polymer polyvinyl alcohol (PVA) was dissolved in 18 mL of deionized water at 60 °C. First, the freestanding PVA

nanofiber network was collected through electrospinning (working voltage of 15 kV and receiving distance of 15 cm) on a home-made frame using Cu wire. Then, metallic silver was covered on the PVA nanofiber network by direct current sputtering (JZCK-580) with a silver target of 99.99 at% to obtain a freestanding AgNF network. Polyethylene terephthalate (PET) substrates were ultrasonically cleaned in ethanol and deionized water for 10 min and then concentrated in a plasma cleaner (HARRICK, PDC-32G-2) to improve surface hydrophilicity. Finally, the freestanding AgNF network has adhered to the PET substrate as a flexible transparent current collector.

2.2.2. Preparation of MoO_3 nanowires. MoO_3 nanowires were synthesized *via* a hydrothermal method. Briefly, 2 g of Mo powder was added into 10 mL of deionized water to form a uniform mixture, followed by slow addition of 20 mL of H_2O_2 (30 wt%) until the solution became light-yellow. The solution was continuously stirred for 30 min and transferred into a stainless steel autoclave lined with para-polyphenol (PPL). The temperature was increased to 220 °C at a heating rate of 4 °C min^{-1}, and the hydrothermal process was maintained at 220 °C for 7 days, followed by natural cooling to room temperature. The obtained powder was repeatedly washed and centrifuged at 5000 rpm for 5 min with deionized water, and the obtained product was centrifuged and washed three times with deionized water and ethanol. Finally, MoO_3 nanowires were annealed at 450 °C for 2 h under an Ar atmosphere.

2.2.3. Preparation of the AMP electrode. MoO_3 nanowires were dispersed into deionized water (10 mg mL^{-1}), and then the PEDOT:PSS solution (1.3–1.7 wt%, Cool Chemical Tech Co.) was added under ultra-sonication for 12 hours to obtain the MoO_3/PEDOT:PSS hybrid dispersion. The concentration of hybrid dispersions was modulated with the precursor volume ratio (MoO_3 nanowire dispersion : PEDOT:PSS solution = 3 : 1–8 : 1). It was found that the optimal ratio was 6 : 1. The AMP film electrode was obtained by spin-coating twice the above-depicted hybrid dispersion on the flexible transparent AgNF network. AgNFs/MoO_3 (AM) and AgNFs/PEDOT:PSS (AP) film electrodes were also fabricated with the same process, using the MoO_3 dispersion and diluted PEDOT:PSS solution (deionized water : PEDOT:PSS solution = 6 : 1), respectively. Finally, all film electrodes were heated at 120 °C for 30 min.

2.3. FTSC fabrication

Transparent PVA/LiCl gel electrolyte was synthesized as follows: 3 g of LiCl and 3 g of PVA were separately added into 30 mL of deionized water, and then heated to 80 °C under vigorous stirring. PVA/LiCl gel electrolyte was cast onto the AMP electrodes. Once the excess water was vaporized, a pair of film electrodes were pressed together to assemble into a symmetric sandwich-structured FTSC device. The fabrication process of the AMP-based FTSCs is illustrated in Scheme 1.

2.4. Characterization

The sample structure was characterized using an X-ray diffraction spectrometer (XRD, X'pert pro, Philips) with Cu Kα radiation (range: 10–70°, step: 0.02° s^{-1}, wavelength: 0.15406 nm) and micro Raman spectroscopy (JY-HR800 micro-Raman, using a 532 nm wavelength YAG laser with a laser spot diameter of ~600 nm and power attenuator of D 0.3). Scanning electron microscopy (SEM, Tescan Mira3) and high-resolution transmission electron microscopy (HRTEM, FEI Tecnai G2 F30) were used to check the morphology and microstructure. An ultraviolet-visible spectrophotometer (U-3900H, HITACHI) recorded the transmittance spectra of film electrodes and devices. The elements and chemical valences were checked on an X-ray photoelectron spectrometer (XPS, PHI-5702, Mg KR X-ray, 1253.6 eV). The bending test of film electrodes and FTSC devices was performed on a measurement system assembled with an electric platform (SJH-500) and KEITHLEY2700.

2.5. Electrochemical measurements

The electrochemical properties of film electrodes were characterized using an electrochemical workstation (CHI 660E) in a three-electrode configuration. The as-prepared film electrode, platinum sheet, and Ag/AgCl electrodes were used as the working, counter, and reference electrodes, respectively. The electrolyte was 2 M Na_2SO_4 aqueous solution. The electrochemical properties of FTSC devices were measured in a two-electrode configuration.

3. Results and discussion

Fig. 1 shows the characterization of the AgNF network and MoO_3 nanowire nanostructures. A randomly orientated centimeter-wide AgNF network was achieved by sputtering metallic Ag on freestanding electro-spun PVA nanofibers (Fig. 1a, S1, and S2†). After the removal of the PVA template, Ag hollow fibers with ~65 nm wall thickness can be seen in Fig. 1a and the inset. The enlarged SEM image in Fig. 1b shows one typical AgNF junction, which largely determines the resistance of the transparent conductive electrodes (TCEs). A close contact generally leads to small sheet resistances of the TCEs. The mean diameter of the obtained AgNFs is found to be 480 nm (Fig. 1c). The hydrothermally synthesized MoO_3 nanowires (Fig. 1d) are 7.9 μm in length and 240 nm in diameter (Fig. S3†). As shown in Fig. 1e, the HRTEM image of MoO_3 nanowires reveals apparent lattice fringes with a spacing distance of 0.35 nm, corresponding to the (002) plane of the α-MoO_3 phase (JCPDS No. 05-0508).[43] Moreover, the selected area electron diffraction (SAED) pattern indicates that the as-synthesized MoO_3 nanowires are monocrystalline (see the inset in Fig. 1e).

Fig. 1f shows the digital image of the MoO_3/PEDOT:PSS hybrid aqueous dispersion. The TEM image of the AMP electrode shows a uniform PEDOT:PSS conducting glue layer with a thickness of 10 nm covering the surface of MoO_3 nanowires (Fig. 1g). The PEDOT:PSS coating "glue" not only provides electron transport pathways and partial capacitance to maximize the charge storage capability but also reduces the contact resistance between the AgNF network and MoO_3 nanowires. The element mapping in Fig. 1h shows that PEDOT:PSS-glued MoO_3 nanowires contain Mo, O, C, and S elements, confirming the successful coating of an ultrathin PEDOT:PSS layer on AMP

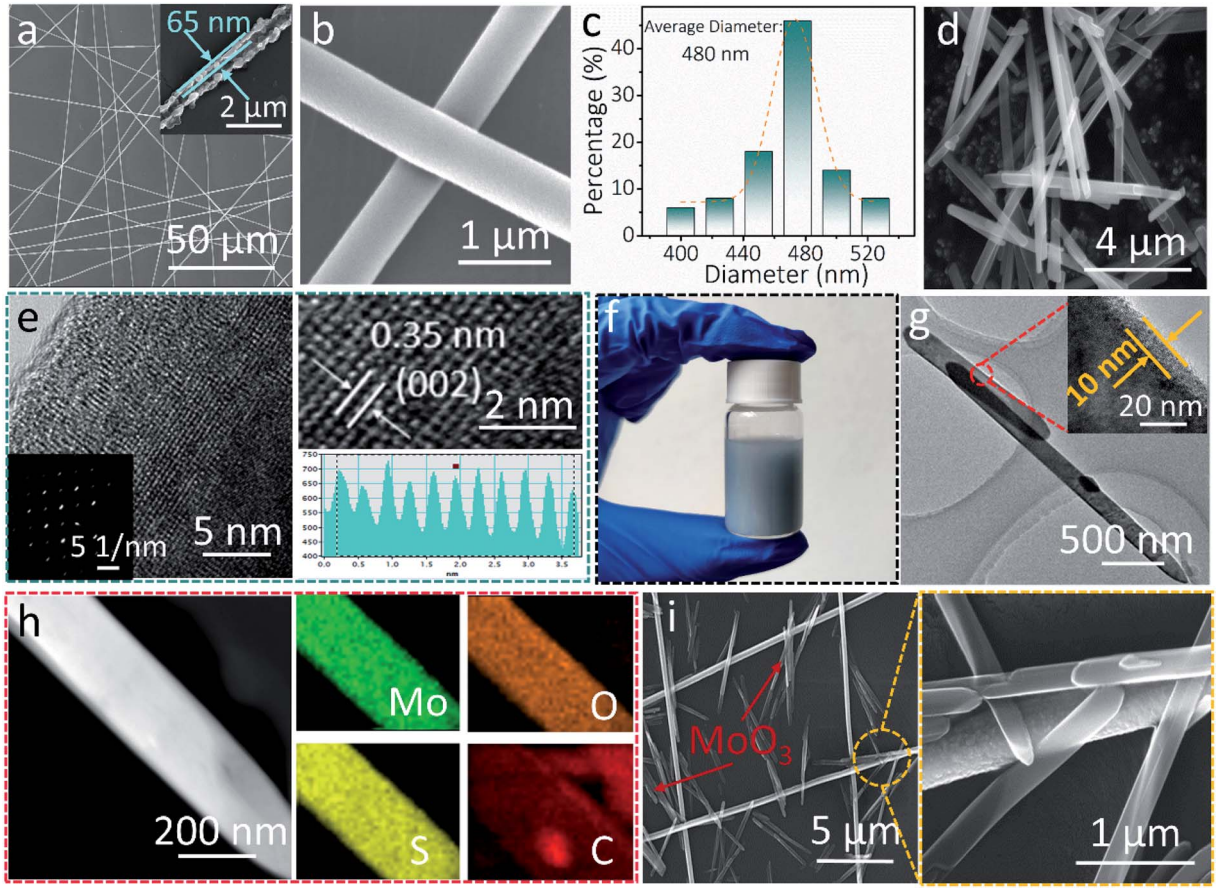

Fig. 1 (a) and (b) SEM images of the AgNF network (inset: SEM image of AgNFs after removing PVA). (c) Diameter histogram of AgNFs. (d) SEM, (e) TEM, and HRTEM images of the as-synthesized MoO_3 nanowires, the inset shows a SAED pattern. (f) Digital image of the MoO_3/PEDOT:PSS dispersion. (g) TEM, HRTEM, and (h) elemental-mapping images of PEDOT:PSS-glued MoO_3 nanowires. (i) SEM image of the AMP electrode.

electrodes. The elemental mapping of MoO_3 nanowires only shows Mo and O elements (Fig. S4†), which also proves the ultrathin PEDOT:PSS layer in the AMP electrodes compared to Fig. 1h. With the assistance of the centrifugal force during the spin-coating, MoO_3 nanowires are firmly anchored on a continuous AgNFs network (Fig. 1i and S5†). One should note that a few MoO_3 nanowires distributed in the interspaces can be connected to the developed AgNF network by PEDOT:PSS to build the integrated film electrode, implying higher utilization of active materials for sequent energy storage compared to the case without PEDOT:PSS "conducting glue".

The XRD pattern (Fig. 2a) and Raman spectrum (Fig. 2b) further verify the formation of the α-MoO_3 phase (JCPDS No. 05-0508).[15,44] According to the XRD data analysis of Fig. 2a, the crystallite size of the MoO_3 nanowire is 39.51 nm. The apparent Raman peaks can be well indexed to the A_g (159, 336, 364, 468, 819 and 997 cm^{-1}), B_{1g} (159, 336, 379, 468, 819, and 997 cm^{-1}), B_{2g} (290 and 666 cm^{-1}), and B_{3g} (129, 245, 290, and 666 cm^{-1}) vibration modes of α-MoO_3.[45,46] As schematically illustrated in Fig. 2c, α-MoO_3 is composed of a bilayer network of edge-sharing MoO_6 octahedra, and these bilayers are piled up along the *c*-axis and bonded to adjacent layers by van der Waals forces.[44] The layered crystal structure is usually suitable for intercalation/de-intercalation of ions with a relatively small ion radius, such as H^+, Li^+, and Na^+.[47] The wide-range XPS survey of PEDOT:PSS-glued MoO_3 nanowires is presented in Fig. S6,† indicating the coexistence of Mo, O, and S elements. The binding energy of Mo $3d_{5/2}$ and Mo $3d_{3/2}$ electron peaks, centered at 232.6 and 235.7 eV, suggests a +6 oxidation state of Mo that is consistent with α-MoO_3 (Fig. 2d and S7†).[48] Fig. 2e exhibits the S 2p core level spectrum, where the peaks located at 167.8 (S $2p_{3/2}$) and 163.5 eV (S $2p_{1/2}$) can be assigned to the sulfur in PEDOT:PSS chains.[49,50] Besides, the O 1s spectrum can be deconvoluted into three appropriate peaks (Fig. 2f). The peak at 530.4 eV corresponds to the bridging oxygen of Mo–O–Mo,[51] whereas the other two peaks at 532.2 and 532.8 eV can be attributed to the oxygen of PEDOT:PSS chains.[49] All these results confirm the successful fabrication of AMP electrodes.

The transparency, conductivity, mechanical flexibility, and electrical stability of the AMP electrode determine the optoelectronic and electrochemical performances of FTSCs. Fig. 3a presents the optical images of the as-prepared transparent AgNF electrode, AMP electrode, and FTSC device, respectively, demonstrating high optical transmittance in all samples. Depositing MoO_3/PEDOT:PSS onto the AgNF network reduces the transmittance of the latter from 93.6% to 82.8% (at 550 nm, Fig. 3b) at the cost of slightly increased sheet resistance (from

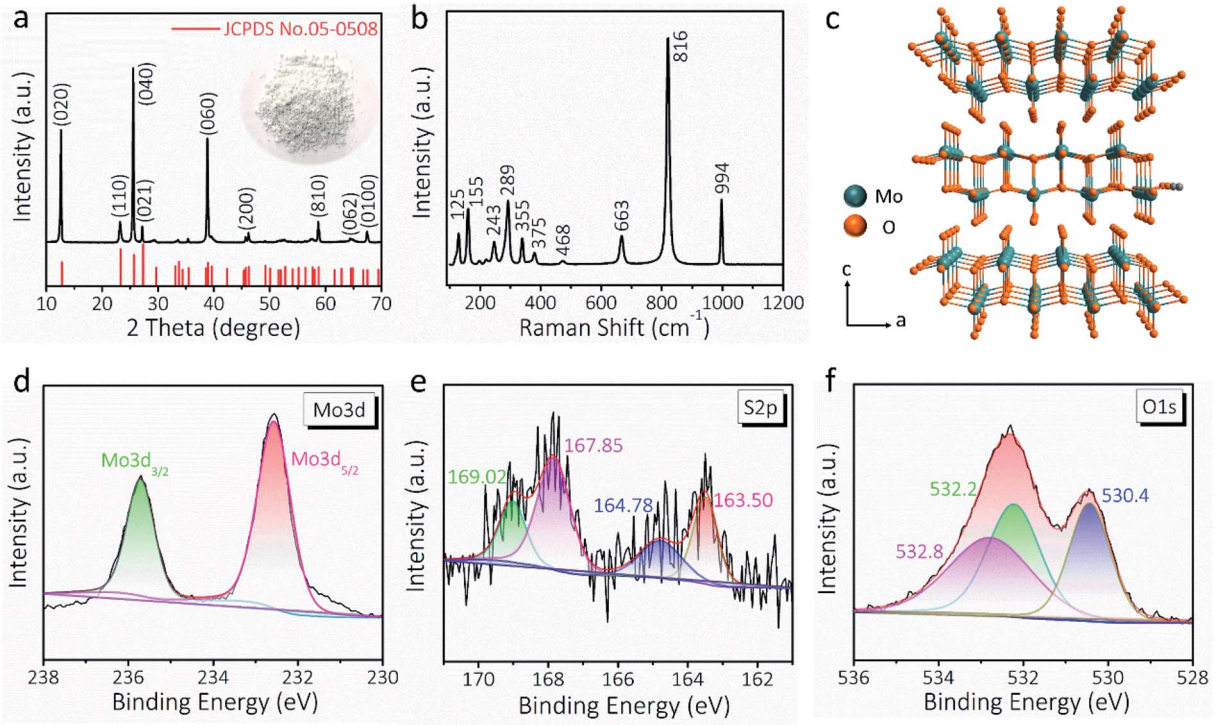

Fig. 2 (a) XRD pattern and (b) Raman spectrum of the as-synthesized MoO_3 nanowires (inset: a digital image of as-synthesized MoO_3 nanowire powder). (c) Schematic diagram of the α-MoO_3 crystal structure. XPS spectra of (d) Mo 3d, (e) S 2p, and (f) O 1s for PEDOT:PSS-glued MoO_3 nanowires.

8.0 Ω sq^{-1} to 9.7 Ω sq^{-1}). The excellent optoelectronic properties (in particular the highly conductive network) can be well attributed to the unique 1D nanofibers/nanowire hybrid electrode structure assisted by the "conducting glue" at the junctions. The as-assembled FTSC device shows a transmittance of 64.5%, which is comparable to those of other reported FTSCs.[2,13,52] It is worth noting that the overall optical transmittance can be further improved by reducing the distribution density or diameter of AgNFs, and/or exploring active materials with low optical conductivity.

The AgNF network, as a current conductor in a circuit, is capable of continuously maintaining a stable LED light during the deformation (Fig. S8†). To demonstrate the flexibility of the as-fabricated TCEs, the relative resistance (R/R_o) of the electrodes is recorded as a function of bending cycles in Fig. 3c. Even after 1000 cycles (bending angle of 90°, curvature radius of 10 mm), the resistance of the AgNF network and AMP electrode remained almost unchanged, indicating superior mechanical flexibility. Moreover, R/R_o values at different bending angles were collected for the AgNF network and AMP electrode (Fig. 3d), showing that the electrical resistance remains extremely stable below the bending angle of 120°, which corresponds to a curvature radius of 6 mm. These results suggested that even after depositing MoO_3/PEDOT:PSS, the flexibility of the ultrathin TCEs has been well maintained. Even bending to 180° (a curvature radius of 2 mm), the resistance of the AMP electrode increases slightly, which can be credited to the role of the conducting glue at the junctions. Notably, the mechanical flexibility of the AMP electrode is much better and the resistance change of the AMP electrode after 1000 bending cycles is much smaller compared to those of previously reported metal network/grid based on Cu nanofibers,[53] AgNWs/PEDOT:PSS,[54] and Ag grid,[55,56] respectively (Table S1†).

The optical transparency and electrochemical properties of AMP electrodes were optimized by adjusting the volume ratio of MoO_3 nanowire dispersion to PEDOT:PSS solution. Fig. 4a shows the transmittance spectra of AMP electrodes with different ratios from 3 : 1 to 8 : 1. The optical transmittance at 550 nm reduces with increasing the precursor ratio (Fig. S9†). The GCD curves at 0.10 mA cm^{-2} for AMP electrodes with different precursor ratios are shown in Fig. 4b. Fig. 4c shows the calculated areal capacitance at 0.10 mA cm^{-2} and FoM_c values for the AMP electrodes with different precursor ratios. As the precursor ratio increases, the calculated areal capacitance by GCD curves reaches a peak value at 6 : 1 (Fig. 4b). A large precursor ratio corresponds to a lower amount of PEDOT:PSS in film electrodes, reducing the electrical conductivity of film electrodes. For transparent AMP film electrodes, the FoM_c is calculated by the ratio of volumetric capacitance to optical conductivity (C_V/σ_{op}).[19]

$$T = \left[1 + \frac{188.5}{C_V}\sigma_{op}C_A\right]^{-2} \quad (1)$$

where T is the optical transmittance and C_A is the intrinsic areal capacitance of the film electrode. The FoM_c (F S cm^{-2}) can be achieved by measuring a series of T and C_A:

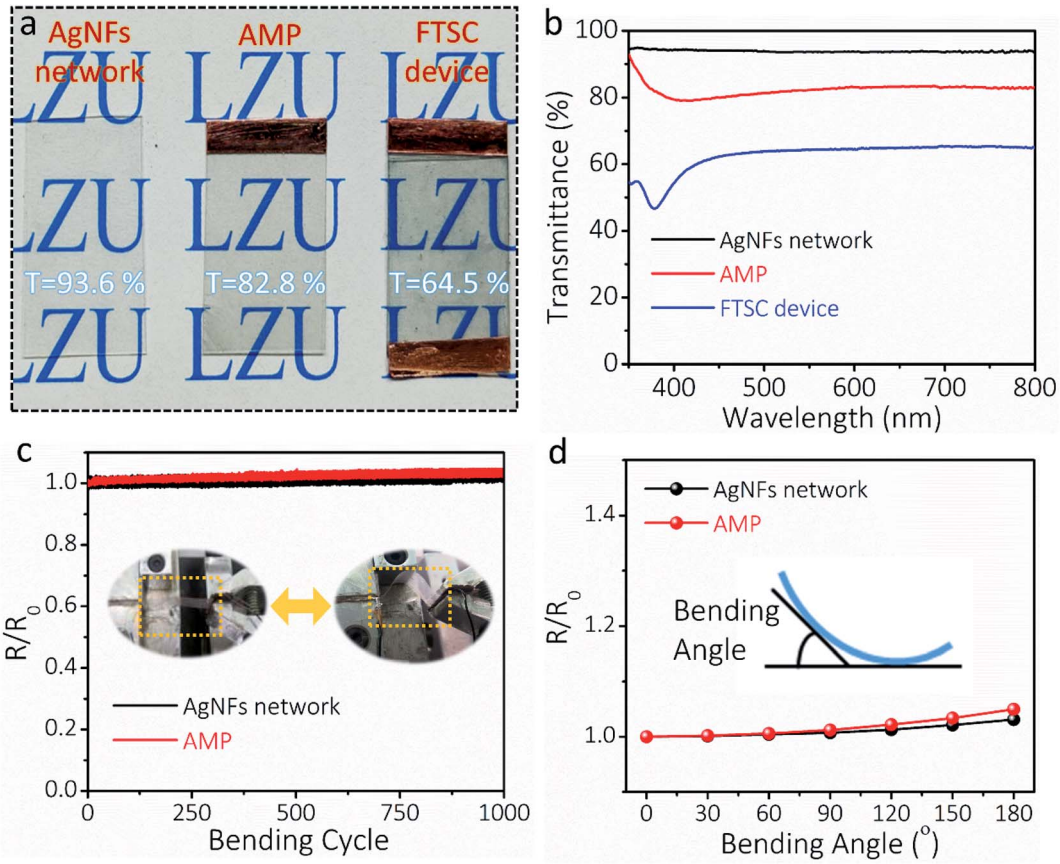

Fig. 3 (a) Digital photographs and (b) transmittance spectra of the AgNF network, AMP electrode and FTSC device, indicating high optical transparency. (c) The relative electrical resistance of the AgNF network and AMP electrode as a function of bending cycles (inset: the bending photograph of AMP electrode). (d) The relative electrical resistance of the AgNF network and AMP electrode as a function of bending angles (inset: bending angle diagram).

$$\mathrm{FoM_C} = \frac{188.5 C_A}{T^{-0.5} - 1} \quad (2)$$

A larger $\mathrm{FoM_c}$ value means better charge storage capability in FTSCs at a given thickness. The AMP electrodes with the precursor ratio of 6 : 1 have the highest $\mathrm{FoM_c}$ of 14.96 F S $\mathrm{cm^{-2}}$. Notably, this value is substantially higher than that of PEDOT:PSS films (1.73 F S $\mathrm{cm^{-2}}$),[12] $\mathrm{MnO_2}$/Au electrodes (7.21 F S $\mathrm{cm^{-2}}$),[38] and $\mathrm{Co_3O_4}$/ITO electrodes (10.2 F S $\mathrm{cm^{-2}}$).[57] Therefore, the optimal 6 : 1 ratio is utilized to evaluate the electrochemical performance of AMP electrodes, unless specifically noted. The transmittance and electrochemical performance of the film electrodes with different spin-coating times, corresponding to different amounts of active materials, are shown in Fig. S10.† Apparently, the contribution from pure AgNFs is negligible, best evidenced by the small CV integrated area compared to those of AMP electrodes (Fig. S10a†). Fig. S11† demonstrates the CVs and the derived capacitance of the AgNF electrode, showing a negligible capacitance (~0.11 mF $\mathrm{cm^{-2}}$) from this TCE that is two orders of magnitude lower than that of AMP electrodes.

To estimate the capacitance contribution of each component in AMP electrodes, cyclic voltammetry (CV) curves (Fig. 4d) of AM, AP, and AMP film electrodes were measured at 10 mV $\mathrm{s^{-1}}$, showing areal capacitances of 2.3, 4.2, and 9.4 mF $\mathrm{cm^{-2}}$, respectively (Fig. 4d). The CV curves and areal capacitances of AM electrodes at different scan rates are shown in Fig. S12.† Besides, an apparent polarization can be observed in the CV curves of AP and AM electrodes, respectively. As the conducting glue-PEDOT:PSS is connected with more $\mathrm{MoO_3}$ nanowires, the AMP electrode shows higher areal capacitances majorly contributed by $\mathrm{MoO_3}$ instead of PEDOT:PSS. The AMP electrode exhibits a quasi-rectangular CV shape due to the synergistic influence of PEDOT:PSS and $\mathrm{MoO_3}$ nanowires, rendering optimal electronic and ionic transport kinetics. Based on the CV curves of the AMP electrode (Fig. S13†), the potential window of −0.8 to 0 V was selected, where the quasi-rectangular shape of the CV curve is maintained without any obvious electrochemical polarization. At the same time, this voltage window is suitable for PEDOT:PSS, since the PEDOT:PSS typically oxidizes during anodic scanning in a high voltage window.

The quasi-rectangular shape of CV curves is maintained up to 100 mV $\mathrm{s^{-1}}$ (Fig. S14†), indicating excellent capacitive behavior and reversible redox reactions. The Faraday redox reactions of $\mathrm{MoO_3}$ nanowires in $\mathrm{Na^+}$ aqueous electrolyte include surface adsorption/desorption (eqn (3)) and intercalation/deintercalation of $\mathrm{Na^+}$ in the interlayer spacing of $\mathrm{MoO_3}$ (eqn (4))[47,58]

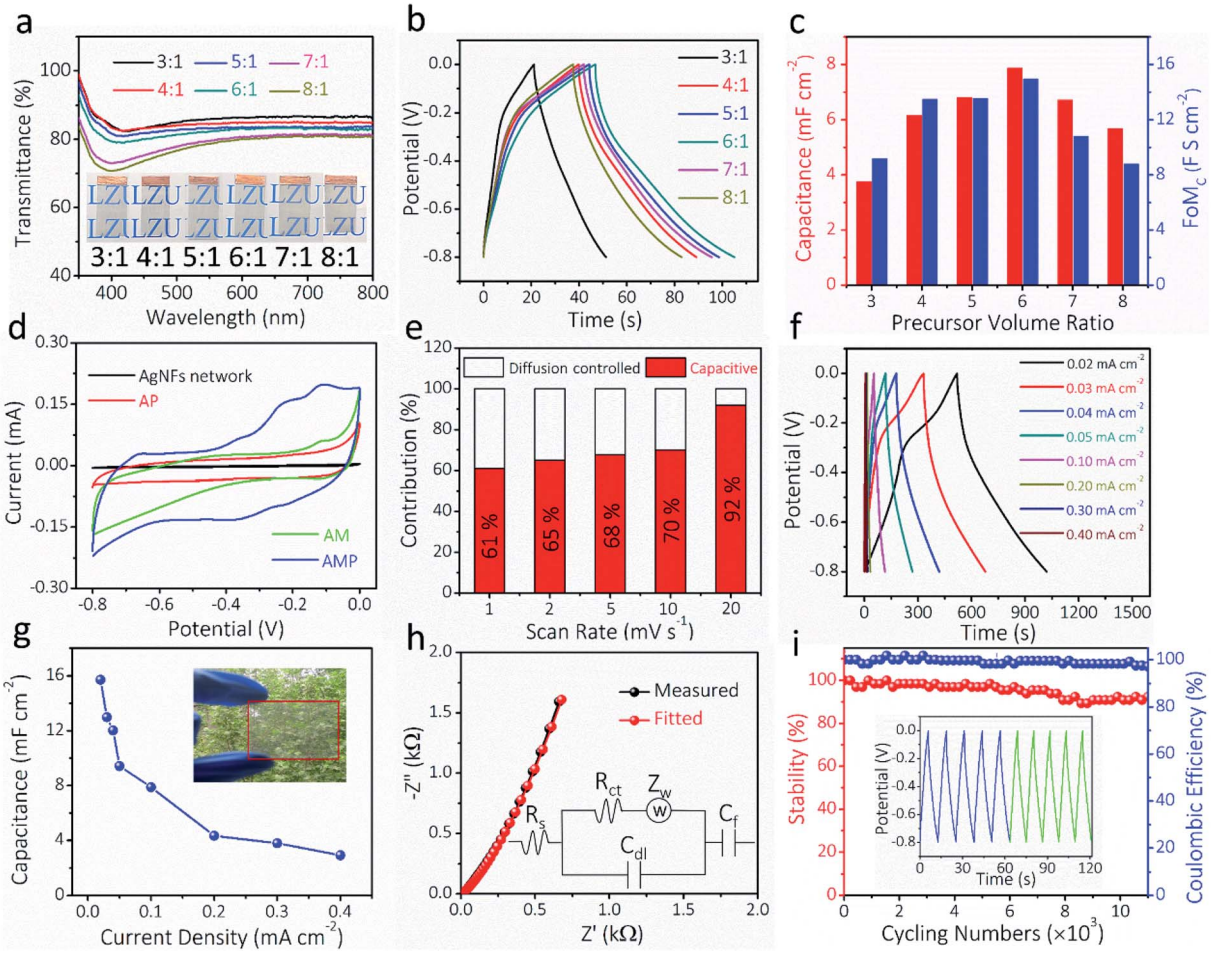

Fig. 4 Electrochemical characterization of flexible transparent AMP electrodes. (a) Optical transmittance of the film electrodes based on different precursor ratios of MoO_3 nanowires to PEDOT:PSS (inset: digital photographs of film electrodes). (b) GCD curves at 0.10 mA cm^{-2} for AMP electrodes with different precursor ratios. (c) Areal capacitances calculated from GCD curves and FoM_c values for the electrodes with different precursor ratios. (d) CV curves at 10 mV s^{-1} for the AgNF network, AP, AM, and AMP film electrodes with the optimal 6 : 1 ratio. (e) Normalized contribution ratio of capacitive capacitance at different scan rates. (f) GCD curves measured at different current densities for the AMP electrode (precursor ratio of 6 : 1). (g) The calculated areal capacitance of AMP electrodes at different current densities (inset: digital photograph of AMP electrode). (h) EIS curves of AMP electrodes, the inset is an equivalent circuit diagram. (i) The electrochemical cycling stability and coulombic efficiency of AMP electrodes, the inset shows the GCD curves of the initial and final five cycles.

$$(Mo^{VI}O_3)_{surface} + Na^+ + e^- \leftrightarrow (Mo^{V}O_3Na)_{surface} \quad (3)$$

$$xNa^+ + yH_2O + MoO_3 + xe^- \leftrightarrow Na_x{}^+(H_2O)_y[MoO_3]^{x-} \quad (4)$$

The electrochemical kinetics of AMP electrodes can be analyzed by the given relationship: $i = av^b$, where a and b are adjustable parameters.[59] When $b = 0.5$, the electrochemical process majorly relies on the diffusion-controlled process, while $b = 1.0$ indicates a capacitive process. Based on the linear relationship between $\log(i)$ and $\log(v)$, we obtained a b-value of 0.83, implying that the capacitive process plays a leading role in the charge storage of AMP electrodes (Fig. S15†). To further analyze the capacitive and diffusion-controlled contributions at different scan rates, the current (i) can be divided into two parts: capacitive effect (k_1v) and diffusion-controlled reaction ($k_2v^{1/2}$).[60] Fig. 4e shows the calculated capacitive and diffusion-controlled capacitance contributions at different scan rates. At 5 mV s^{-1}, 68% of the total charge can be assigned to the capacitive process (Fig. S16†). The contribution from the capacitive-controlled process steadily increases with the enhancement of scan rates, which becomes dominant up to 20 mV s^{-1}.

GCD curves and the derived capacitances at different current densities for the AMP electrode are shown in Fig. 4f–g. The maximum areal capacitance is 15.7 mF cm^{-2} at 0.02 mA cm^{-2}, which is much higher than those of the previously reported FTSC electrodes, such as graphene,[13] PEDOT:PSS/metal mesh,[61] $Co(OH)_2$/AgNWs,[2] MnO_2/metal mesh,[30] and MXenes[24] at similar optical transparency. Electrochemical impedance spectroscopy (EIS) was carried out to explore the ion diffusion/transport capability and electrical conductivity of AMP electrodes. As shown in Fig. 4h, the extracted equivalent series resistance (R_s) value is as low as 6.5 Ω, which proves the outstanding electrical transport behavior of AMP electrodes. Also, the steep curve in

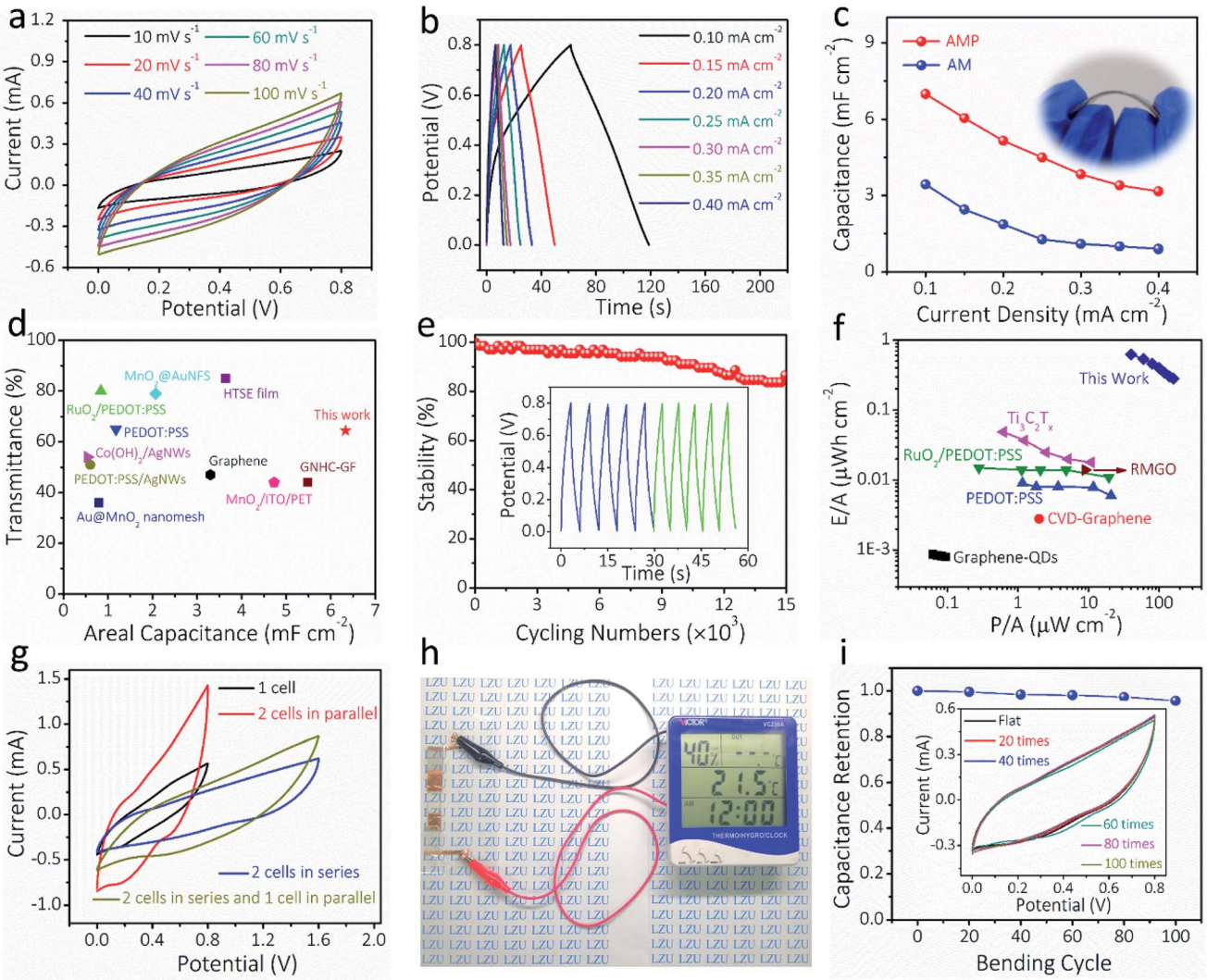

Fig. 5 Electrochemical characterization of the assembled all-solid-state FTSCs based on AMP electrodes. (a) CV curves at different scan rates and (b) GCD curves at different current densities for the AMP-based FTSCs. (c) The calculated areal capacitance obtained from GCD curves (inset: digital photograph of the AMP-based FTSC device). (d) The areal capacitance and optical transmittance compared with the other reported FTSCs. The detailed values are presented in Table S2.† (e) Electrochemical cycling stability of the FTSC, the inset shows the GCD curves of the initial and the final five cycles. (f) Ragone plots of the FTSC, compared with the other reported ones. The detailed values are presented in Table S3.† (g) CV curves of the FTSC devices at different configurations. (h) A digital photograph showing that three FTSCs in series can power a multifunction thermometer. (i) The electrochemical performance of the FTSC device during the bending, the inset shows CV curves of the FTSC at 50 mV s^{-1} after different bending times.

the low-frequency range suggests excellent electrochemical capacitive behavior. The long-term stability of AMP electrodes is evaluated through the GCD test at 0.30 mA cm^{-2}, showing a capacitance retention of 92.4% after 11 000 charge/discharge cycles (Fig. 4i). The inset in Fig. 4i compares the GCD curves of the initial five cycles (blue) and the final five ones (green), confirming the excellent stability of the electrode. The excellent cycling performance could be attributed to (i) the unique nanofibers/nanowire hybrid electrode structure, which guarantees the optimal electronic/ionic transport kinetics, and (ii) PEDOT:PSS conducting glue, covered on MoO_3 nanowires, which effectively ensures an excellent electrical contact between MoO_3 nanowires and the AgNF current collector and maximizes the charge storage capability. Furthermore, the coulombic efficiency of AMP electrodes is close to 100%, implying the absence of any parasitic reactions during repeated GCD cycles.

To demonstrate the potential of AM and AMP electrodes in practical applications, all-solid-state symmetric FTSCs were assembled with PVA/LiCl as the gel electrolyte and separator. Fig. 5a presents the CV curves of the AMP-based FTSC device measured varying from 10 to 100 mV s^{-1}. The almost quasi-rectangular CV shapes are well maintained up to 100 mV s^{-1}, indicating pseudo-capacitive behaviors and rapid charge/discharge capability, which can also be verified by the GCD curves in Fig. 5b. The GCD curve of the FTSC device measured with a potential window of 0 to 0.8 V under different applied current densities exhibited a typical symmetric triangular shape, indicating good electrochemical capacitive

characteristics (Fig. 5b). The symmetric charge/discharge curves of the device also indicate a relatively high coulombic efficiency. The areal capacitance of the FTSC is exhibited in Fig. 5c. A large areal capacitance of 7.0 mF cm^{-2} is achieved at 0.1 mA cm^{-2} of the AMP-based FTSC device, which is significantly higher than those of previously reported FTSCs.[2,13,52] The areal capacitance of the AMP-based FTSC device is doubled compared to the AM-based FTSC device (Fig. S17†), highlighting the importance of PEDOT:PSS as the conducting glue. It is undeniable that PEDOT:PSS has a certain capacitance contribution. Hence, the expected combination of high transmittance and large capacitance has been achieved in our as-prepared AMP-based FTSC devices (Fig. 5d and Table S2†). The acquired EIS comparison results also demonstrate that the AMP-based FTSCs render a low internal resistance and fast ionic diffusion (Fig. S18†). Moreover, the FTSCs exhibit excellent long-term cycling stability (Fig. 5e), retaining 86.6% of the initial capacitance after 15 000 charge/discharge cycles. As shown in Fig. 5f, the energy density (0.623 μW h cm^{-2}) and power density (40 μW cm^{-2}) of the AMP-based FTSC device have also outperformed the previously reported transparent supercapacitors, such as $Ti_3C_2T_x$ films,[24] PEDOT:PSS,[12] RuO_2/PEDOT:PSS,[18] graphene quantum-dot,[62] CVD-graphene[63] and multilayer reduced graphene oxide thin films.[63] (Table S3†) To meet practical applications, the required voltage and capacitance can be achieved *via* a simple serial-parallel configuration. Fig. 5g shows CV curves of a single device and two identical devices connected in either parallel or series configurations. The operated potential window can be enlarged from 0.8 to 1.6 V by connecting two devices in series, whereas the output current density (*i.e.* capacitance) can be increased twice by connecting two devices in parallel. Moreover, the GCD curves of tandem devices are consistent with the results of CV curves (Fig. S19†). Also, three tandem transparent devices can readily drive a multifunction thermometer (Fig. 5h), showcasing promising applications of our flexible transparent supercapacitors in powering portable electronics. Besides, the CV curves of the AMP-based FTSC device were measured at 50 mV s^{-1} when the device was bent at different angles (Fig. S20†). After 100 bending cycles at 90° (Fig. 5i), almost no decrease in capacitance was observed, implying the robust nature of our fabricated transparent solid-state devices. These attractive properties, including the very high figure of merit (charge storage), excellent optoelectronic properties in combination with mechanical resilient and electrochemical performances, suggest the great promise of AMP-based FTSCs in next-generation transparent, wearable electronics.

4. Conclusions

In summary, we have designed an AMP film electrode for an advanced transparent, flexible supercapacitor device. The PEDOT:PSS functions as "conducting glue" between the highly conductive AgNF network and high-theoretical capacitance MoO_3 nanowires, resulting in much enhanced electron hopping kinetics and improved mechanical adhesion of the active materials. These synergistic effects render a high areal capacitance of 15.71 mF cm^{-2} at an optical transparency of 82.8% in the AMP film electrodes, coupled with long-term electrochemical cycle stability (92.4% capacitance retention after 11 000 charge/discharge cycles) and excellent mechanical flexibility (withstanding 1000 bending cycles). More importantly, the AMP-based all-solid-state symmetric FTSCs also exhibit large capacitance, high energy density, superior power density, and long-term cycling stability. These results indicate the great potential of nanofibers/nanowire hybrid network structures in high-performance transparent, wearable, and portable electronics.

Author contributions

Jie Liang: conceptualization, methodology, data curation, writing – original draft, investigation, visualization, validation. Hongwei Sheng: investigation, methodology, writing – review & editing. Qi Wang: investigation. Jiao Yuan: methodology. Xuetao Zhang: methodology. Qing Su: writing – review & editing. Erqing Xie: supervision. Wei Lan: writing – review & editing, funding acquisition, project administration, resources, supervision. Chuanfang (John) Zhang: conceptualization, data curation, writing – review & editing.

Conflicts of interest

The authors declare no conflicts of interest.

Acknowledgements

This work was supported by the National Natural Science Foundation of China (61874166 and U1832149) and the Science and Technology Program of Qinghai Province (2020-HZ-809).

Notes and references

1 C. F. Zhang and V. Nicolosi, *Energy Storage Materials*, 2019, **16**, 102–125.
2 H. Sheng, X. Zhang, Y. Ma, P. Wang, J. Zhou, Q. Su, W. Lan, E. Xie and C. J. Zhang, *ACS Appl. Mater. Interfaces*, 2019, **11**, 8992–9001.
3 H. Zhou, Y. Zhang, Y. Qiu, H. Wu, W. Qin, Y. Liao, Q. Yu and H. Cheng, *Biosens. Bioelectron.*, 2020, **168**, 112569.
4 C. Zhang, Z. Peng, C. Huang, B. Zhang, C. Xing, H. Chen, H. Cheng, J. Wang and S. Tang, *Nano Energy*, 2021, **81**, 105609.
5 C. F. Zhang, M. Y. Liang, S. H. Park, Z. F. Lin, A. Seral-Ascaso, L. L. Wang, A. Pakdel, C. O. Coileain, J. Boland, O. Ronan, N. McEvoy, B. G. Lu, Y. G. Wang, Y. Y. Xia, J. N. Coleman and V. Nicolosi, *Energy Environ. Sci.*, 2020, **13**, 2124–2133.
6 J. Xiong, L. M. Pan, H. H. Wang, F. Du, Y. M. Chen, J. Yang and C. F. Zhang, *Electrochim. Acta*, 2018, **268**, 503–511.
7 H. Tang, W. L. Li, L. M. Pan, K. J. Tu, F. Du, T. Qiu, J. Yang, C. P. Cullen, N. McEvoy and C. F. Zhang, *Adv. Funct. Mater.*, 2019, **29**, 1901907.
8 G. Yasin, M. Arif, T. Mehtab, M. Shakeel, M. A. Mushtaq, A. Kumar, T. A. Nguyen, Y. Slimani, M. T. Nazir and H. H. Song, *Inorg. Chem. Front.*, 2020, **7**, 402–410.

9 S. Ullah, G. Yasin, A. Ahmad, L. Qin, Q. Yuan, A. U. Khan, U. A. Khan, A. U. Rahman and Y. Slimani, *Inorg. Chem. Front.*, 2020, **7**, 1750–1761.
10 Y. Slimani and E. Hannachi, in *Nanobatteries and Nanogenerators*, ed. H. Song, R. Venkatachalam, T. A. Nguyen, H. B. Wu and P. Nguyen-Tri, Elsevier, 2021, pp. 343–363, DOI: 10.1016/B978-0-12-821548-7.00013-0.
11 T. Chen, Y. Xue, A. K. Roy and L. Dai, *ACS Nano*, 2014, **8**, 1039–1046.
12 T. M. Higgins and J. N. Coleman, *ACS Appl. Mater. Interfaces*, 2015, **7**, 16495–16506.
13 N. Li, G. Yang, Y. Sun, H. Song, H. Cui, G. Yang and C. Wang, *Nano Lett.*, 2015, **15**, 3195–3203.
14 Y. H. Liu, J. L. Xu, S. Shen, X. L. Cai, L. S. Chen and S. D. Wang, *J. Mater. Chem. A*, 2017, **5**, 9032–9041.
15 B. Yao, L. Huang, J. Zhang, X. Gao, J. Wu, Y. Cheng, X. Xiao, B. Wang, Y. Li and J. Zhou, *Adv. Mater.*, 2016, **28**, 6353–6358.
16 K. Seevakan, A. Manikandan, P. Devendran, Y. Slimani, A. Baykal and T. Alagesan, *J. Magn. Magn. Mater.*, 2019, **486**, 165254.
17 Y. Slimani and E. Hannachi, in *Hybrid Perovskite Composite Materials*, eds. I. Khan, A. Khan, M. M. A. Khan, S. Khan, F. Verpoort and A. Umar, Woodhead Publishing, 2021, pp. 335–354, DOI: 10.1016/B978-0-12-819977-0.00016-0.
18 C. F. Zhang, T. M. Higgins, S. H. Park, S. E. O'Brien, D. H. Long, J. Coleman and V. Nicolosi, *Nano Energy*, 2016, **28**, 495–505.
19 L. B. Wang and X. L. Hu, *Batteries Supercaps*, 2020, **3**, 1–13.
20 S. Sollami Delekta, A. D. Smith, J. Li and M. Östling, *Nanoscale*, 2017, **9**, 6998–7005.
21 D. S. Hecht, L. Hu and G. Irvin, *Adv. Mater.*, 2011, **23**, 1482–1513.
22 J. Ge, G. Cheng and L. Chen, *Nanoscale*, 2011, **3**, 3084–3088.
23 E. Senokos, M. Rana, M. Vila, J. Fernandez-Cestau, R. D. Costa, R. Marcilla and J. J. Vilatela, *Nanoscale*, 2020, **12**, 16980–16986.
24 C. J. Zhang, B. Anasori, A. Seral-Ascaso, S. H. Park, N. McEvoy, A. Shmeliov, G. S. Duesberg, J. N. Coleman, Y. Gogotsi and V. Nicolosi, *Adv. Mater.*, 2017, **29**, 1702678.
25 P. Salles, E. Quain, N. Kurra, A. Sarycheva and Y. Gogotsi, *Small*, 2018, **14**, 1802864.
26 S. Abdolhosseinzadeh, R. Schneider, A. Verma, J. Heier, F. Nuesch and C. F. Zhang, *Adv. Mater.*, 2020, **32**, 2000716.
27 C. F. Zhang, L. F. Cui, S. Abdolhosseinzadeh and J. Heier, *Infomat*, 2020, **2**, 613–638.
28 S. Abdolhosseinzadeh, J. Heier and C. F. Zhang, *JPhys Energy*, 2020, **2**, 031004.
29 A. W. Lang, Y. Y. Li, M. De Keersmaecker, D. E. Shen, A. M. Osterholm, L. Berglund and J. R. Reynolds, *ChemSusChem*, 2018, **11**, 854–863.
30 S. B. Singh, T. I. Singh, N. H. Kim and J. H. Lee, *J. Mater. Chem. A*, 2019, **7**, 10672–10683.
31 X. Jiao, C. Zhang and Z. Yuan, *ACS Appl. Mater. Interfaces*, 2018, **10**, 41299–41311.
32 H. Moon, H. Lee, J. Kwon, Y. D. Suh, D. K. Kim, I. Ha, J. Yeo, S. Hong and S. H. Ko, *Sci. Rep.*, 2017, **7**, 41981.
33 R. T. Wang, X. B. Yan, J. W. Lang, Z. M. Zheng and P. Zhang, *J. Mater. Chem. A*, 2014, **2**, 12724–12732.
34 H. B. Lee, W. Y. Jin, M. M. Ovhal, N. Kumar and J. W. Kang, *J. Mater. Chem. C*, 2019, **7**, 1087–1110.
35 S. Gong, Y. M. Zhao, Q. Q. Shi, Y. Wang, L. W. Yap and W. L. Cheng, *Electroanal*, 2016, **28**, 1298–1304.
36 Y. Lee, S. Chae, H. Park, J. Kim and S. H. Jeong, *Chem. Eng. J.*, 2020, **382**, 122798.
37 Y. Wang, S. Gong, D. Dong, Y. Zhao, L. W. Yap, Q. Shi, T. An, Y. Ling, G. P. Simon and W. Cheng, *Nanoscale*, 2018, **10**, 15948–15955.
38 S. Kiruthika, C. Sow and G. U. Kulkarni, *Small*, 2017, **13**, 1701906.
39 S. Q. Chen, B. B. Shi, W. D. He, X. Y. Wu, X. Zhang, Y. B. Zhu, S. He, H. H. Peng, Y. Jiang, X. S. Gao, Z. Fan, G. F. Zhou, J. M. Liu, K. Kempa and J. W. Gao, *Adv. Funct. Mater.*, 2019, **29**, 1906618.
40 Y. Slimani, A. Selmi, E. Hannachi, M. A. Almessiere, M. Mumtaz, A. Baykal and I. Ercan, *J. Mater. Sci.: Mater. Electron.*, 2019, **30**, 13509–13518.
41 S. B. Singh, T. Kshetri, T. I. Singh, N. H. Kim and J. H. Lee, *Chem. Eng. J.*, 2019, **359**, 197–207.
42 T. Cheng, Y. Z. Zhang, J. D. Zhang, W. Y. Lai and W. Huang, *J. Mater. Chem. A*, 2016, **4**, 10493–10499.
43 S. Balendhran, J. Deng, J. Z. Ou, S. Walia, J. Scott, J. Tang, K. L. Wang, M. R. Field, S. Russo, S. Zhuiykov, M. S. Strano, N. Medhekar, S. Sriram, M. Bhaskaran and K. Kalantar-zadeh, *Adv. Mater.*, 2013, **25**, 109–114.
44 S. N. Lou, Y. H. Ng, C. Ng, J. Scott and R. Amal, *ChemSusChem*, 2014, **7**, 1934–1941.
45 G. Mestl, P. Ruiz, B. Delmon and H. Knozinger, *J. Phys. Chem.*, 1994, **98**, 11269–11275.
46 J. Zhou, N. S. Xu, S. Z. Deng, J. Chen, J. C. She and Z. C. Wang, *Adv. Mater.*, 2003, **15**, 1835–1840.
47 J. B. Jiang, J. L. Liu, S. J. Peng, D. Qian, D. M. Luo, Q. Wang, Z. W. Tian and Y. C. Liu, *J. Mater. Chem. A*, 2013, **1**, 2588.
48 Z. Chen, D. Cummins, B. N. Reinecke, E. Clark, M. K. Sunkara and T. F. Jaramillo, *Nano Lett.*, 2011, **11**, 4168–4175.
49 D. A. Mengistie, M. A. Ibrahem, P. C. Wang and C. W. Chu, *ACS Appl. Mater. Interfaces*, 2014, **6**, 2292–2299.
50 Y. Xia, K. Sun and J. Ouyang, *Adv. Mater.*, 2012, **24**, 2436–2440.
51 J. C. Dupin, D. Gonbeau, P. Vinatier and A. Levasseur, *Phys. Chem. Chem. Phys.*, 2000, **2**, 1319–1324.
52 T. Qiu, B. Luo, M. Giersig, E. M. Akinoglu, L. Hao, X. Wang, L. Shi, M. Jin and L. Zhi, *Small*, 2014, **10**, 4136–4141.
53 H. Wu, L. Hu, M. W. Rowell, D. Kong, J. J. Cha, J. R. McDonough, J. Zhu, Y. Yang, M. D. McGehee and Y. Cui, *Nano Lett.*, 2010, **10**, 4242–4248.
54 R. T. Ginting, M. M. Ovhal and J. W. Kang, *Nano Energy*, 2018, **53**, 650–657.
55 S. Hong, J. Yeo, G. Kim, D. Kim, H. Lee, J. Kwon, H. Lee, P. Lee and S. H. Ko, *ACS Nano*, 2013, **7**, 5024–5031.
56 Y. Lee, W. Y. Jin, K. Y. Cho, J. W. Kang and J. Kim, *J. Mater. Chem. C*, 2016, **4**, 7577–7583.

57 X. Y. Liu, Y. Q. Gao and G. W. Yang, *Nanoscale*, 2016, **8**, 4227–4235.
58 I. Shakir, M. Nadeem, M. Shahid and D. J. Kang, *Electrochim. Acta*, 2014, **118**, 138–142.
59 J. Liu, J. Wang, C. Xu, H. Jiang, C. Li, L. Zhang, J. Lin and Z. X. Shen, *Adv. Sci.*, 2018, **5**, 1700322.
60 H. S. Kim, J. B. Cook, H. Lin, J. S. Ko, S. H. Tolbert, V. Ozolins and B. Dunn, *Nat. Mater.*, 2017, **16**, 454–460.
61 X. Liu, D. Li, X. Chen, W. Y. Lai and W. Huang, *ACS Appl. Mater. Interfaces*, 2018, **10**, 32536–32542.
62 K. Lee, H. Lee, Y. Shin, Y. Yoon, D. Kim and H. Lee, *Nano Energy*, 2016, **26**, 746–754.
63 J. J. Yoo, K. Balakrishnan, J. Huang, V. Meunier, B. G. Sumpter, A. Srivastava, M. Conway, A. L. Reddy, J. Yu, R. Vajtai and P. M. Ajayan, *Nano Lett.*, 2011, **11**, 1423–1427.